The role of acoustic nonlinearity in tissue heating behind a rib cage using a high-intensity focused ultrasound phased array

2013 Phys. Med. Biol. 58 2537

(http://iopscience.iop.org/0031-9155/58/8/2537)

IOP Publishing Physics in Medicine and Biology

Phys. Med. Biol. **58** (2013) 2537–2559 doi:10.1088/0031-9155/58/8/2537

The role of acoustic nonlinearity in tissue heating behind a rib cage using a high-intensity focused ultrasound phased array

Petr V Yuldashev[1,2], Svetlana M Shmeleva[1], Sergey A Ilyin[1], Oleg A Sapozhnikov[1,3], Leonid R Gavrilov[4] and Vera A Khokhlova[1,3,5]

[1] Physics Faculty, Moscow State University, Moscow 119991, Russia
[2] Ecole Centrale de Lyon, Centre Acoustique, 36 Av. Guy de Collongue, F-69134 Ecully Cedex, France
[3] Center for Industrial and Medical Ultrasound, APL, University of Washington, SA 98105, USA
[4] N.N. Andreyev Acoustics Institute, Moscow 117036, Russia

E-mail: vera@acs366.phys.msu.ru

Received 9 November 2012, in final form 27 February 2013
Published 26 March 2013
Online at stacks.iop.org/PMB/58/2537

Abstract

The goal of this study was to investigate theoretically the effects of nonlinear propagation in a high-intensity focused ultrasound (HIFU) field produced by a therapeutic phased array and the resultant heating of tissue behind a rib cage. Three configurations of focusing were simulated: in water, in water with ribs in the beam path and in water with ribs backed by a layer of soft tissue. The Westervelt equation was used to model the nonlinear HIFU field, and a 1 MHz phased array consisting of 254 circular elements was used as a boundary condition to the model. The temperature rise in tissue was modelled using the bioheat equation, and thermally necrosed volumes were calculated using the thermal dose formulation. The shapes of lesions predicted by the modelling were compared with those previously obtained in *in vitro* experiments at low-power sonications. Intensity levels at the face of the array elements that corresponded to the formation of high-amplitude shock fronts in the focal region were determined as 10 W cm^{-2} in the free field in water and 40 W cm^{-2} in the presence of ribs. It was shown that exposures with shocks provided a substantial increase in tissue heating, and its better spatial localization in the main focal region only. The relative effects of overheating ribs and splitting of the focus due to the periodic structure of the ribs were therefore reduced. These results suggest that utilizing nonlinear propagation and shock formation effects can be beneficial for inducing confined HIFU lesions when irradiating through obstructions such as ribs. Design of compact therapeutic arrays to provide maximum power outputs with lower intensity levels at the elements

[5] Author to whom any correspondence should be addressed.

is necessary to achieve shock wave regimes for clinically relevant sonication depths in tissue.

1. Introduction

High-intensity focused ultrasound (HIFU) is an emerging medical technology capable of transcutaneous thermal ablation of target sites within an mm-sized focal region without damaging intervening tissues. While HIFU has been shown to be successful for the treatment of a range of tumours in different organs, including liver, uterus, kidney and prostate (Wu *et al* 2004, Hesley *et al* 2008, Ritchie *et al* 2010, Crouzet *et al* 2010, Dubinsky *et al* 2008), a number of challenges that limit its even broader clinical application still remain. One of these challenges is related to the HIFU irradiation of the liver and heart, which are partially shielded by the rib cage. The presence of ribs, which are strongly reflecting, aberrating and absorbing obstacles for ultrasound, results in the degradation of beam focusing, insufficient heating of the targeted tissue and overheating bones and overlying tissue layers, including skin (Wu *et al* 2004, Civale *et al* 2006, Li *et al* 2006).

Methods which use multi-element phased arrays, the operation of whose elements is optimized to irradiate mostly through intercostal spaces and thus to minimize the ultrasound impact on the ribs, have been proposed. The principle of one group of such methods is to switch off the elements that are located in the geometrical shade of the ribs when viewed from the focal point (Botros *et al* 1998, Liu *et al* 2007, Bobkova *et al* 2010, Quesson *et al* 2010). More rigorous approaches include the calculation of the optimized amplitude and phase distribution for the elements to account for diffraction effects, tissue and bone inhomogeneous structure and scattering from ribs (Aubry *et al* 2008, Cochard *et al* 2009, Gélat *et al* 2011). It has been shown, both in simulation and experiment, that such optimizations provide significant reduction in the heating of the ribs. However, application of the methods is not technically simple and the presence of ribs still results in the degradation of focusing. For example, diffraction effects due to the regular structure of ribs can result in the splitting of the focus and the appearance of the side foci, leading to an additional $\sim$50% reduction of the intensity in the main focus and undesired hot spots in tissue (Khokhlova *et al* 2010, Bobkova *et al* 2010).

Use of nonlinear propagation effects in exposures through obstructions such as ribs in addition to the modulation of the operation of array elements, or even without such modulation, could be beneficial. Intensity levels in the focal region of HIFU beams can reach thousands of W cm^{-2} (Wu *et al* 2004) leading to a strong distortion of an acoustic waveform in the focal region. At these intensity levels, high-amplitude shock fronts develop in the focus and significantly alter the *in situ* exposure conditions (Bailey *et al* 2003, Canney *et al* 2008). Recent experimental and modelling results give evidence that shock fronts do form in HIFU fields in tissue (Canney *et al* 2010). These shocks are focused into very small volumes and thus produce very effective and localized heating. Heat deposition at the focus in tissue caused by absorption at shocks of 50–100 MPa amplitude is several tens times higher than heating from linear focusing with the same initial intensity (Filonenko and Khokhlova 2001, Canney *et al* 2010). The presence of shocks not only accelerates thermal ablations but also enables mechanical fractionation or emulsification of tissue using the so-called cavitation-cloud histotripsy (Parsons *et al* 2006, Maxwell *et al* 2011) or boiling histotripsy (Canney *et al* 2009, Khokhlova *et al* 2011a) pulsing schemes. In addition, nonlinear effects accumulate on the way to the focus and are mainly present in the central focal lobe, where pressures are the highest. Nonlinear enhancement of heating therefore has a much weaker effect in the field close to the transducer, i.e. near skin and ribs, and in the additional lower amplitude

side lobes in the focal region (Khokhlova *et al* 2011b). It was shown recently that tissue damage in the secondary lobes caused by cavitation effects in histotripsy sonication through ribs was also minimized if acoustic pressure in the main lobe exceeded the cavitation threshold and the secondary lobes remained below the threshold (Kim *et al* 2011). There is a promise therefore that more confined lesions can be generated using shock waves even in the absence of aberration correction at the array elements.

In order either to utilize or to avoid shock wave exposures using HIFU arrays when irradiating through ribs, it is therefore important to evaluate the degree of nonlinear effects and determine the power output levels at which shocks develop in the focus for a specific HIFU array. Numerical modelling validated against measurement has been shown to serve as a powerful tool for characterizing nonlinear HIFU fields in water and for predicting *in situ* values of an acoustic field in tissue (Canney *et al* 2008, Bessonova *et al* 2009). However, to date most studies that analyse shock formation exposures have been carried out for axially symmetric single-element transducers based on the KZK equation (Filonenko and Khokhlova 2001, Khokhlova *et al* 2002, Khokhlova *et al* 2006, Canney *et al* 2008, Bessonova *et al* 2009); the effect of ribs has been considered in a weakly nonlinear, and low focusing gain, field using 3D KZK modelling (Li *et al* 2007). When the radiator is not a single-element spherical source but a multi-element 2D phased array, the modelling approach is technically much more difficult as the simulation of 3D nonlinear fields with shocks requires parallel programming and large resources of computer memory. A more accurate diffraction model is also necessary to account for the wide spatial spectrum of the array field adequately. Recently, a fully 3D model based on the Westervelt equation has been developed and applied to the modelling of the field of a clinical multi-element array HIFU transducer (Yuldashev and Khokhlova 2011). The results of simulations have been validated against measurements and have shown that the technical parameters of the array allowed shock formation regimes in the focus in water (Kreider *et al* 2011). It was shown that for this particular array, shock fronts form in the focus in water at the clinically relevant intensity level of 5 W cm^{-2} at the array elements. The maximum intensity values for modern HIFU transducers can reach 30–40 W cm^{-2}, thus leaving additional power available to compensate for absorption in tissue on the way to the focus (Cathignol 2002, Fleury *et al* 2002). However, the results for potential shock wave exposures are currently available for only one array and the effect of the presence of ribs has not been evaluated.

The goal of this paper was to investigate the significance of nonlinear effects in an HIFU beam generated by another typical HIFU array with and without ribs. The acoustic field of this array has been previously characterized in water at low output levels, i.e. in linear focusing regimes (Hand *et al* 2009). Acoustic wave propagation through a rib cage and the ability to produce thermal lesions in *ex vivo* porcine tissue placed behind the rib phantom have also been considered in modelling and experiment (Bobkova *et al* 2010). The ribs were represented as absolutely absorbing parallel strips; acoustic field modelling was based on the Rayleigh integral calculation and was limited by the linear approximation. The bioheat equation and thermal dose formulation were used to determine the size and the shape of lesions produced under these linear exposure conditions and the results of modelling were validated against experimental data (Ilyin *et al* 2011). Here, the 3D Westervelt model (Yuldashev and Khokhlova 2011) was generalized to simulate nonlinear propagation through ribs under the same geometrical configuration of sonications as in the previous paper (Bobkova *et al* 2010). Two modes of operating the array elements were compared: when all elements were switched on and when some elements were switched off to minimize the heating effect on ribs. Nonlinear modelling was first performed in water at increasing acoustic output levels, then in water in the presence of ribs on the way to focus and finally when focusing through

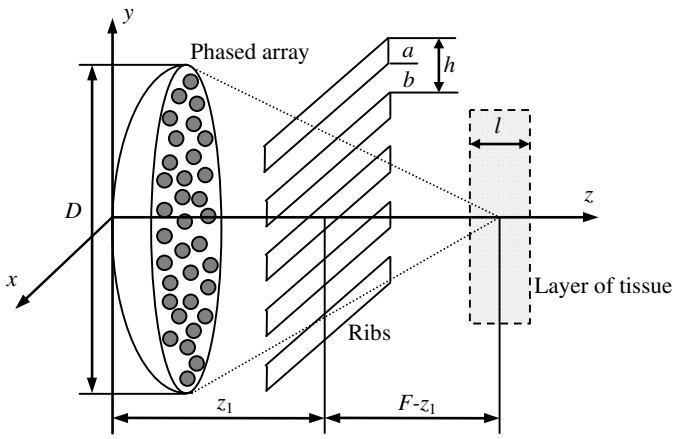

Figure 1. Geometry of nonlinear ultrasound field model generated by an HIFU array, and focusing through ribs into a layer of tissue.

the ribs inside a layer of tissue. Output levels of the array at which shock fronts developed in the focus were determined. The spatial structure of the HIFU field and enhancement of tissue heating by shocks were analysed. Various regimes of heating that utilize nonlinear effects were considered. The shapes of lesions predicted in the modelling were compared with those previously obtained in *in vitro* experiments at low-power sonications (Bobkova *et al* 2010).

2. Materials and methods

2.1. Therapeutic phased array with random distribution of elements

The phased array, used in simulations, consisted of 254 circular elements, each of diameter 7 mm and operational frequency 1 MHz. The elements were distributed on a spherical surface in a quasi-random manner. The minimum centre-to-centre spacing between the elements was 7.9 mm and the largest spacing was 9.4 mm. A radius of curvature of the spherical shell and its diameter were $F = 130$ mm and $D = 170$ mm, respectively. A central hole of 40 mm diameter was provided for the insertion of an imaging transducer. The active area of the array was 100 cm^2. The array was developed according to the design and parameters described in Gavrilov and Hand (2000). More details about the array construction could be found in Hand *et al* (2009).

2.2. Numerical simulation of the nonlinear acoustic field of the array

The method developed for the calculation of the nonlinear acoustic field of a therapeutic phased array has been reported previously by Yuldashev and Khokhlova (2011). In the present paper, it is generalized for the case when ribs and tissue are present. Simulations were performed for three configurations of the propagation medium following the methodology described below. For all configurations, pressure waveforms, distributions of intensity, peak pressures and heat deposition rates (in the case of focusing in a tissue layer) were calculated in the focal region of the beam.

The geometry of focusing is shown in figure 1. No electronic steering of the focus was considered, and thus the focus was always located at the centre of curvature of the array surface. The initial pressure distribution was first reconstructed in the initial plane $z = 0$ mm

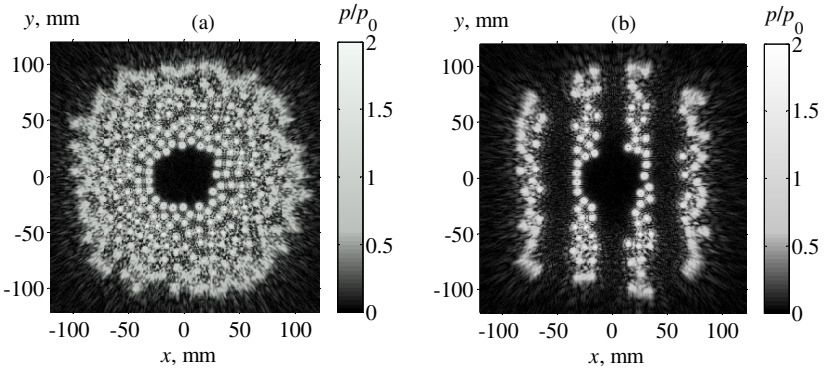

Figure 2. Pressure distributions reconstructed in the plane $z = 0$ to use as boundary conditions for nonlinear acoustic simulation of the field generated by the array. (a) All the elements of the array are switched on. (b) Some elements of the array are switched off to minimize the ultrasonic impact on ribs. The distributions are normalized to the characteristic initial pressure amplitude p_0 at the face of each element.

by applying the Rayleigh integral to the radiating elements, located at the spherical surface of the array (Yuldashev and Khokhlova 2011). This pressure distribution (figure 2(a)) was used as a boundary condition to the 3D Westervelt equation (Westervelt 1963). The equation was written in a retarded coordinate system to model the forward propagation of acoustic waves in the direction to the focus:

$$\frac{\partial^2 p}{\partial \tau \partial z} = \frac{c_0}{2}\Delta p + \frac{\beta}{2\rho_0 c_0^3}\frac{\partial^2 p^2}{\partial \tau^2} + \frac{\alpha_w}{2c_0^3}\frac{\partial^3 p}{\partial \tau^3} + L_t(p). \tag{1}$$

Here p is the acoustic pressure, z is the coordinate along the axis of the array, $\tau = t - z/c_0$, t is the time coordinate, $\Delta = \partial^2/\partial z^2 + \partial^2/\partial y^2 + \partial^2/\partial x^2$ is the Laplacian in all spatial coordinates, x and y are the transverse spatial coordinates, ρ_0 is the density, c_0 is the ambient sound speed in the medium, α_w is the parameter of thermoviscous absorption in water, L_t is the additional absorption term in tissue and β is the coefficient of nonlinearity in the medium.

The linear operator L_t, which models additional absorption in tissue, governs the linear power law of absorption with frequency and the corresponding dispersion according to the equations

$$\alpha_t(\omega) = \alpha_{t0}\frac{\omega}{\omega_0}, \qquad \frac{c(\omega) - c_0}{c_0} = \frac{2c_0\alpha_{t0}}{\pi\omega_0}\ln\left(\frac{\omega}{\omega_0}\right). \tag{2}$$

Here, c_0 is the sound speed and α_{t0} is the absorption coefficient at the fundamental frequency $f_0 = \omega_0/2\pi$ of ultrasound (O'Donnell *et al* 1981, Kashcheeva *et al* 2000).

Simulations were conducted using the combined spectral and time domain representations of the solution for the pressure field. In the spectral domain, the pressure was represented as a Fourier series expansion using a finite number of harmonics:

$$p(\tau, x, y, z) = 1/2 \cdot \sum_{n=-N_{\max}}^{N_{\max}} p_n(x, y, z) \cdot \exp(-i\omega_0 n\tau). \tag{3}$$

Here, p_n is the pressure amplitude of the nth harmonic in the numerical solution of equation (1), and $N_{\max}$ is the maximum number of harmonics included in simulations. The number $N_{\max}$ was varied over the propagation distance depending on the degree of distortion of the pressure waveform. The initial number of $N_{\max}$ at $z = 0$ was 10 and its maximum value in the focal region was 500. The transition between the spectral and temporal representations of the solution was carried out using a fast Fourier transform (FFT) from the FFTW library.

The Westervelt equation (1) was integrated over the propagation coordinate z using the method of fractional steps with a second-order operator-splitting algorithm for different physical effects: nonlinearity, diffraction and absorption/dispersion. Two algorithms were employed to calculate the nonlinear term of the equation. In the first algorithm, a set of coupled nonlinear equations (Filonenko and Khokhlova 2001) for the amplitudes of harmonics, p_n, was integrated using the Runge–Kutta method with a fourth order of accuracy (Press *et al* 2007). This algorithm was used in the nearfield of the beam, before the formation of shocks in the pressure waveform, as it is effective for a small number of harmonics (up to several tens). At distances closer to the focus, where shock fronts developed, a conservative Godunov-type time domain scheme, which allowed accurate capture of the evolution of strongly distorted waveforms using a small number of grid points at the shocks, was used.

The diffraction term of equation (1) was calculated for each harmonic p_n using the angular spectrum method (Zemp *et al* 2003). To reduce the reflections from the boundaries in the x and y directions, an artificial absorption quadratic with frequency was introduced in the layer adjacent to the boundaries of the spatial domain. The absorption and dispersion terms were calculated in the frequency domain using the exact solutions for each harmonic p_n (Filonenko and Khokhlova 2001).

The spatial distributions of ultrasound field intensity were reconstructed from the distributions of the amplitudes of harmonics in the quasi-plane wave approximation as

$$I = \frac{1}{2\rho_0 c_0} \sum_{n=1}^{N_{\max}} |p_n|^2, \tag{4}$$

where $|p_n|$ is the absolute value of the complex pressure amplitude of the nth harmonic (3).

Following the approach used in the previous study (Yuldashev and Khokhlova 2011), the boundary condition to the model (1) was set at the plane $z = 0$ as a pressure distribution determined from the vibrations of the array elements distributed over the spherical shell. The pressure distribution was first calculated at the plane $z = 2$ cm using the Rayleigh integral and assuming that the elements are spherically curved circular pistons having the same magnitude V_0 of the vibration velocity at their faces. Then, the distribution was back-projected to the plane $z = 0$ using the angular spectrum method. The characteristic values of the initial pressure amplitude p_0 and intensity I_0 were introduced as $p_0 = \rho_0 c_0 V_0$ and $I_0 = p_0^2/2\rho_0 c_0$, respectively.

In the first configuration, free field propagation in water was considered at increasing pressure levels I_0 at the array element faces. All the elements of the array were switched on and neither ribs nor tissue was present in the acoustic beam path. Pressure fields were calculated on a 3D rectangular grid in the volume defined by $0 \leqslant z \leqslant 160$ mm axially; x and y within the same spatial windows from -135 mm to $+135$ mm with spatial steps $\mathrm{d}z = \lambda/20 = 0.075$ mm and $\mathrm{d}x = \mathrm{d}y = \lambda/75 = 0.02$ mm, where $\lambda = 1.5$ mm is the wavelength in water for 1 MHz frequency. Simulations were conducted for linear ($\beta = 0$ in (1)) and nonlinear ($\beta = 3.5$) focusing for the intensity levels at the elements $I_0 = 1$, 5 and 10 W cm^{-2}. Pressure waveforms calculated at each grid point of the focal region were analysed to determine the initial intensity value I_0 at which a shock front forms in the focus. The distributions of peak positive p_+ and peak negative p_- pressures were reconstructed along the z-axis and in the focal plane $z = F$ from the calculated pressure waveforms. Acoustic parameters for simulations in water were chosen as $\rho_0 = 1000$ kg m^{-3}, $c_0 = 1500$ m s^{-1}, $\beta = 3.5$ and $\alpha_0 = 4.3 \times 10^{-6}$ m^2 s^{-1}.

In the second set of simulations, ribs were present in the beam path as shown in figure 1. Following the model of previous papers (Bobkova *et al* 2010, Ilyin *et al* 2011), the ribs were represented as infinitely thin and absolutely absorbing parallel stripes. This simplified model does not account for actual 3D shapes of the ribs that would affect the overall diffraction and scattering field from the ribs. However, the condition of absolute absorption at the stripes

seems to be adequate as it includes both the known strong absorption of ribs and the scattering effects in the backward direction. The width of each rib was $a = 18$ mm, the width of the intercostal space was $b = 14$ mm and the plane of the ribs was at $z_1 = 45$ mm from the centre of the array. Two boundary conditions were set for the modelling: when all the elements were switched on as in the previous free field simulations (figure 2(a)) and when the elements located opposite ribs were switched off (figure 2(b)), to minimize the ultrasound impact on ribs as described in Bobkova *et al* (2010). The corresponding boundary conditions calculated in the plane $z = 0$ for these two operational modes of the array are shown in figure 2.

The distribution of the operating elements was obtained following the geometric approach: the focus was connected with the centres of each element by straight lines (rays). If the ray intersected a rib, the element was switched off; otherwise it operated with the same amplitude as without ribs. In the simulations, the intensity at the surface of each element was $I_0 = 1$, 5, 10, 20, 30 and 40 W cm^{-2}. Pressure distributions in the focal region in the case of the presence of ribs were calculated in two steps. In the first step, the pressure field was simulated from the plane $z = 0$ up to the plane z_1 of the ribs. Then, the pressure amplitude in the plane z_1 on the ribs was set to zero. The resulting pressure distribution within the intercostal spaces was used as a boundary condition for further calculations towards the focal region. The same spatial windows and grid steps as in the free field modelling were used in simulations.

In the third set of simulations, a soft tissue layer was added to the model in the focal region of the beam as shown in figure 1. The layer of tissue was 20 mm thick and was located between the parallel planes $z = 120$ and 140 mm. The elements of the array were considered to be partially switched off in the same pattern as for the second case of simulations of propagation through the ribs in water only (figure 2(b)). This configuration corresponded to experimental conditions considered in the earlier paper (Bobkova *et al* 2010), where tissue heating at low output levels of sonications was investigated. The acoustic pressure field and heat deposition were calculated in tissue using the parameters $\rho_0 = 1000$ kg m^{-3}, $c_0 = 1500$ m s^{-1}, $\beta = 4.7$ and $\alpha_{t0} = 4.84$ m^{-1} (Duck 1990, Meaney *et al* 2000, Ilyin *et al* 2011). As the sound speed and density chosen in tissue were the same as in water, no reflections from the water/tissue interface were included in the simulations. The intensity at the elements was $I_0 = 2.5$, 5, 10, 20, 30 and 40 W cm^{-2}. The lowest intensity of $I_0 = 2.5$ W cm^{-2} corresponded to the experimental conditions (Bobkova *et al* 2010).

2.3. Temperature and thermal dose modelling in the soft tissue behind the ribs

In order to simulate the temperature rise in tissue induced by the HIFU beam, the bioheat equation

$$\frac{\partial T}{\partial t} = \chi \Delta T + \frac{Q}{c_v} \tag{5}$$

was solved. Here, T is the temperature in tissue as a function of space and time, the initial temperature in tissue was $T_0 = 35\ ^\circ$C, $c_v = 3.06 \times 10^6$ J m^{-3} $^\circ$C^{-1} is the specific heat capacity per unit volume and $\chi = 1.93 \times 10^{-7}$ m^2 s^{-1} is the thermal diffusivity. Heat deposition Q in tissue was calculated from the results of nonlinear acoustic field modelling:

$$Q = \frac{\sum_{n=1}^{N_{\max}} (\alpha_w n^2 + \alpha_{t0} n) \cdot |p_n|^2}{\rho_0 c_0}, \tag{6}$$

as a combination of absorption of each harmonic component of the wave.

The layer of tissue in the calculations was assumed to be thick enough that no temperature rise occurred at the outer boundary of the layer (i.e. $T = T_0$). In the simulations of temperature

(5), an explicit two-step finite-difference scheme of second-order accuracy in time and space was used. The temperature distribution in tissue was calculated for a given radiated power of the array and irradiation time (exposure). The threshold for thermal damage of tissue was determined in accordance with the magnitude of thermal dose defined for the reference temperature of 56 °C (Hill *et al* 2004):

$$t_{56} = \int_0^{t_{\text{heat}}} R_0^{(56-T(t))} dt \geqslant 1. \tag{7}$$

The integration was performed over the whole heating period t_{heat} (expressed in seconds); here T is the temperature (°C) of tissue, $R_0 = 0.5$ for temperatures over 43 °C and $R_0 = 0.25$ for temperatures less than 43 °C (Sapareto and Dewey 1984). The quantity t_{56} is the time equivalent of thermal dose (expressed in seconds); the value of $t_{56} = 1$ s corresponds to the threshold of destruction of tissue which is equivalent to the threshold of $t_{43} = 140$ min (Dewey 1994, Daum and Hynynen 1998, Filonenko *et al* 2004). The reference temperature of 56 °C in calculating the thermal dose (7) was adopted as suggested in Hill *et al* (2004) because this temperature and corresponding equivalent time t_{56} are more relevant to HIFU conditions, rather than 43 °C and t_{43}, typical for low-temperature hyperthermia conditions.

2.4. Continuous and pulse-periodic regimes of tissue heating

In order to evaluate the efficiency of nonlinear effects in tissue heating behind the ribs, two different temporal regimes of HIFU exposures were considered: continuous (cw) irradiation and pulse-periodic schemes. In both regimes, the parameters of irradiation were chosen so that the maximum temperature in tissue did not exceed 100 °C over the course of heating, because thermal effects in tissue modelled by equation (3) do not include boiling. Continuous mode was examined first and HIFU was switched on until the maximum temperature modelled in tissue reached 100 °C. The results of linear and nonlinear modelling were compared. Time to boil was determined, and temperature distributions and regions of thermal lesions at the time of initiation of boiling were analysed for different intensities at the array element faces.

The second regime was chosen as a pulse-periodic scheme, similar to those used for boiling histotripsy exposures, but assuming the shorter duration of pulses so as not to reach boiling in tissue (Khokhlova *et al* 2011a). The exposure parameters were chosen so that the time-average power of the array was the same, with an increase in the peak power within each pulse being compensated for by the pulse duration, i.e. a lower duty factor (Khokhlova *et al* 2006). The total energy irradiated within one repetition period of pulses in the high-amplitude (nonlinear) regime was therefore the same as that in the continuous low-amplitude (linear) regime with the initial intensity $I_0 = 2.5$ W cm^{-2}. The duty factor was 0.125 for an intensity of $I_0 = 20$ W cm^{-2} and 0.0625 for 40 W cm^{-2}. The pulse repetition time was assumed to be sufficiently short that heating could be averaged over a repetition period of the scheme. When nonlinear effects are absent, the time-average intensity is constant and thermal effects are the same for all peak intensities. When nonlinear effects become strong and shock fronts form, the enhancement of ultrasound absorption at the shocks and a more rapid increase of temperature should be observed in high-pressure regions.

3. Results

3.1. Linear and nonlinear acoustic field distributions produced by the phased array in water

First, consider the results of the numerical simulation of the acoustic field in water. All the elements of the array were switched on, and no ribs were located in the ultrasound beam path.

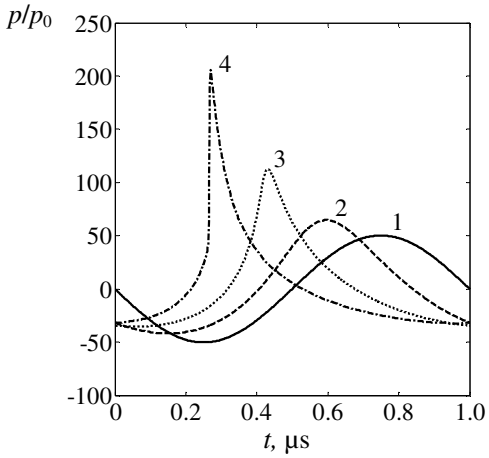

Figure 3. Comparison of one cycle of the focal waveforms in a linear beam (solid curve 1) and nonlinear beams simulated in a free field in water at $I_0 = 1$ W cm^{-2} (curve 2), $I_0 = 5$ W cm^{-2} (curve 3) and $I_0 = 10$ W cm^{-2} (curve 4), where I_0 is the intensity at the array elements. All the elements of the array are switched on and no ribs are present at the beam path. The waveforms are normalized to the characteristic initial pressure amplitude p_0 at the face of each element and are artificially shifted by 0.15 μs relative to each other for better separation.

Figure 3 shows the comparison of focal waveforms (at $z = F$, $x = y = 0$) for the case of linear focusing (solid curve 1) and in nonlinear beams for different initial intensity values at the array elements: $I_0 = 1$ W cm^{-2} (curve 2), $I_0 = 5$ W cm^{-2} (curve 3) and $I_0 = 10$ W cm^{-2} (curve 4). The waveforms were normalized using the initial pressure at the array elements $p_0 = \rho_0 c_0 V_0$. The results showed that strong nonlinear waveform distortion and formation of a shock front are observed for the highest initial intensity of $I_0 = 10$ W cm^{-2}. For initial intensities I_0 below 10 W cm^{-2}, the waveforms exhibit nonlinear distortions with asymmetric compression and rarefaction phases, but shock fronts are not yet produced.

Figure 4 represents peak positive and peak negative pressure distributions along the z-axis (a) and in the focal plane (b) along the y-axis ($x = 0$). The distributions are normalized to the initial pressure values at the array elements. The solid curves marked (1) correspond to the linear beam simulations, while the dashed curves are the results of nonlinear simulations for $I_0 = 1$ W cm^{-2} (2), $I_0 = 5$ W cm^{-2} (3) and $I_0 = 10$ W cm^{-2} (4). Again, the distributions here are normalized using the initial pressure amplitude at the elements of the array. The results show that the focusing gain for the peak positive pressure in the nonlinear beam, $G_{p+} = p_+(F)/p_{0,}$ increases at higher array outputs in comparison with the linearly predicted gain G: $G_{p+} = 1.3G$, $2.2G$ and $4.1G$ for $I_0 = 1$, 5 and 10 W cm^{-2}, respectively. The length and the width of the focal region of p_+ decrease with the growth of the initial intensity from 1 to 10 W cm^{-2}: the dimensions of the -6 dB level change from 1.6 to 0.5 mm along the y-axis and from 8.7 to 4.0 mm along the z-axis. In contrast to the peak positive pressure, the distribution of the peak negative pressure becomes longer and wider: the dimensions of the -6 dB level changes from 8.7 to 10.6 mm along the z-axis and from 1.6 to 2 mm in the focal plane.

The spatial 2D distributions for the peak positive and peak negative pressures are shown in more detail in figure 5 for the linear beam (a) and strongly nonlinear case ((b), (c)) simulated at $I_0 = 10$ W cm^{-2}. In the linear beam (figure 5(a)), the peak positive and peak negative pressure distributions are identical. In the nonlinear case, classical nonlinear-diffraction effects are observed: the peak positive distribution is much more localized in space (figure 5(b)); in contrast, the distribution of the peak negative pressure is enlarged (figure 5(c)) (Bessonova

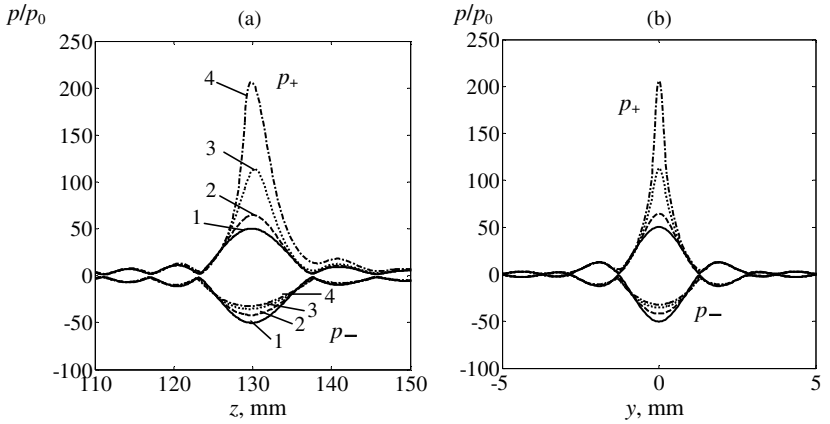

Figure 4. Peak positive and peak negative pressure distributions along the z-axis (a) and in the focal plane (b) along the y-axis ($x = 0$). The distributions are calculated for linear beam focusing (1) and for nonlinear focusing for initial intensity at the array elements $I_0 = 1$ W cm^{-2} (2), $I_0 =$ 5 W cm^{-2} (3) and $I_0 = 10$ W cm^{-2} (4). The distributions are normalized by the initial pressure amplitude $p_0 = \rho_0 c_0 V_0$.

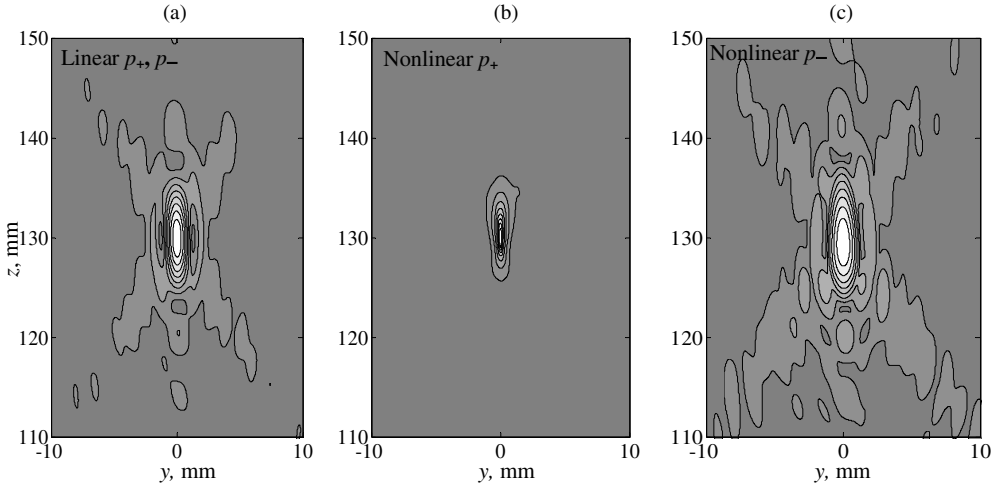

Figure 5. Spatial distributions of the peak positive and peak negative pressures in an axial plane $x = 0$ in a linear (a) and nonlinear (b, c) field of the array. Nonlinear peak positive and peak negative pressure distributions are calculated for $I_0 = 10$ W cm^{-2}. The distributions are normalized by the maximum value for each quantity. The plots contain eight contours equally distributed from the maximum to minimum pressure levels in each plot.

et al 2009). The distribution of the array elements is discrete and non-uniform, and thus some small degree of asymmetry of the field is observed along the transverse y-coordinate for lower pressure level contours. However, the focal region at the pressure levels higher than −6 dB is practically symmetric.

The spatial 2D distributions for the peak positive and peak negative pressures are shown in more detail in figure 5 for the linear beam (a) and strongly nonlinear case ((b), (c)) simulated at $I_0 = 10$ W cm^{-2}. In the linear beam (figure 5(a)), the peak positive and peak negative pressure distributions are identical. In the nonlinear case, classical nonlinear-diffraction effects are observed: the peak positive distribution is much more localized in space (figure 5(b)); in

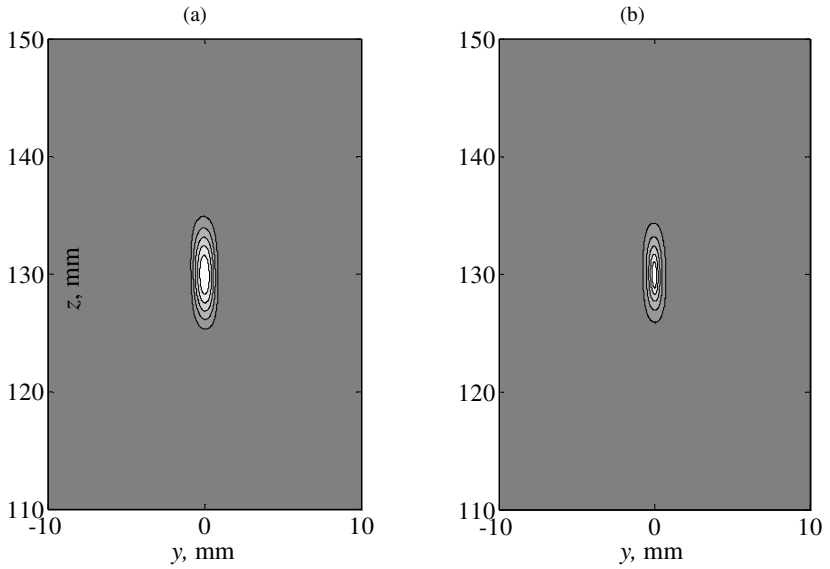

Figure 6. Spatial distributions of intensity in the x-plane of in a linear (a) and nonlinear (b) field of the array. The nonlinear case was calculated at $I_0 = 10$ W cm^{-2}. The distributions are normalized by the maximum value for each plot. The plots contain five contours equally distributed from the maximum to minimum intensity level in each plot.

contrast, the distribution of the peak negative pressure is enlarged (figure 5(c)) (Bessonova *et al* 2009). The distribution of the array elements is discrete and non-uniform, and thus some small degree of asymmetry of the field is observed along the transverse y-coordinate for lower pressure level contours. However, the focal region at the pressure levels higher than -6 dB is practically symmetric.

A characteristic difference in the acoustic pressure distributions in a linear and nonlinear ($I_0 = 10$ W cm^{-2}) beam focusing is also noticeable in the corresponding intensity distributions shown in figure 6. Their widths at the zero–zero level are practically the same in the z- and y-directions. At the -6 dB level the intensity beam width changes from 1.6 to 1.2 mm along the y-axis and from 8.7 to 7.3 mm along the z-axis.

3.2. Effect of ribs on acoustic field distributions produced by the phased array in water

Intensity distributions in the focal plane for the case of linear focusing of the array field in the presence and absence of ribs are compared in figure 7. The distributions are normalized to the initial value of intensity I_0 at the array elements. If all elements are switched on, and ultrasound propagates in water with no ribs present, then the intensity distribution in the focal plane contains a single high-amplitude central peak (curve 1). When ribs are present in the plane $z_1 = 45$ mm, the intensity level in this focal peak decreases by a factor of 5 (curve 2). The reason for this effect is twofold. The first reason is the screening of acoustic beam power by ribs. For the axial position of the rib plane considered here and their size, approximately 56% of all irradiated energy is absorbed by the ribs. The second reason is the focal splitting effect caused by the periodic structure of ribs. The splitting leads to a significant decrease of the focusing gain of the transducer as the total power in each of the side foci is about 50% of that in the main focus. The diffraction nature of this phenomenon has been discussed in detail in previous papers (Bobkova *et al* 2010, Khokhlova *et al* 2010).

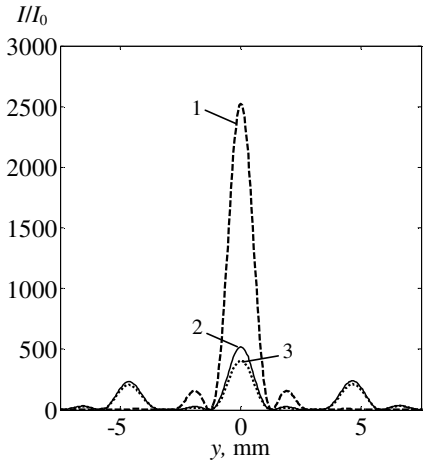

Figure 7. Intensity distributions in the focal plane along the y-axis ($x = 0$) transverse to the rib direction. The distributions were calculated in water for all elements switched on and no ribs present (curve 1), when all elements are switched on and ribs are in beam path (curve 2) and when ribs are present but some elements switched off to minimize the ultrasound impact on ribs (curve 3). The distributions were normalized by the element intensity I_0, and ultrasound propagation was considered as linear.

If the elements of the array screened by the ribs are turned off using the simplest geometric procedure and the rest of the elements operate at the same intensity level I_0, then the ribs are better protected from HIFU heating. The power losses on the ribs in this case were only 25% of the total array power, i.e. more than two times less compared to the case of all elements operating, which were 56% (Bobkova *et al* 2010). However, by switching these elements, additional distortions were introduced in the field distribution in the focal region (figure 7, curve 3). The intensity in the central maximum is decreased by a factor of 1.3. This means that irradiation from the elements located against the ribs provided a non-negligible contribution to the field in the central focus.

The distributions of the peak positive and peak negative pressure along the z-axis (left column) and in the focal plane along the y-axis (right column) are analysed in figure 8. Both the cases of all array elements switched on (dashed lines), and with shadowed elements switched off (solid lines) are presented in the figure. The distributions are calculated in the presence of ribs for different intensity outputs of the array, i.e. for different degrees of nonlinear effects. Plots (a) and (b) correspond to linear focusing of the field. Focal splitting caused by the periodic structure of the ribs is observed in the focal plane (b) with the amplitude of the secondary maximum reaching 75% of the peak pressure value in the central focus. As the peak intensity in the central focus of the linear beam decreased by more than a factor of 4 in the presence of ribs (figure 7), it was expected that amplitude-dependent nonlinear effects would become significant for an initial intensity value close to $I_0 = 40$ W cm^{-2} compared to $I_0 = 10$ W cm^{-2} in the case of free field focusing in water without ribs (figure 2). The results of this case ($I_0 = 40$ W cm^{-2}) and the case of moderate nonlinear effects ($I_0 = 20$ W cm^{-2}) are shown in figures 8(c)–(f). The asymmetry of the distributions for the peak positive and negative pressures is observed for both initial intensities, which indicates that nonlinear effects are already present, but only in the main focal lobe where the pressure is the highest. The asymmetry of the peak pressure distributions in the secondary foci is almost unnoticeable, indicating that nonlinear effects are weak in these regions. Similar to the linear focusing

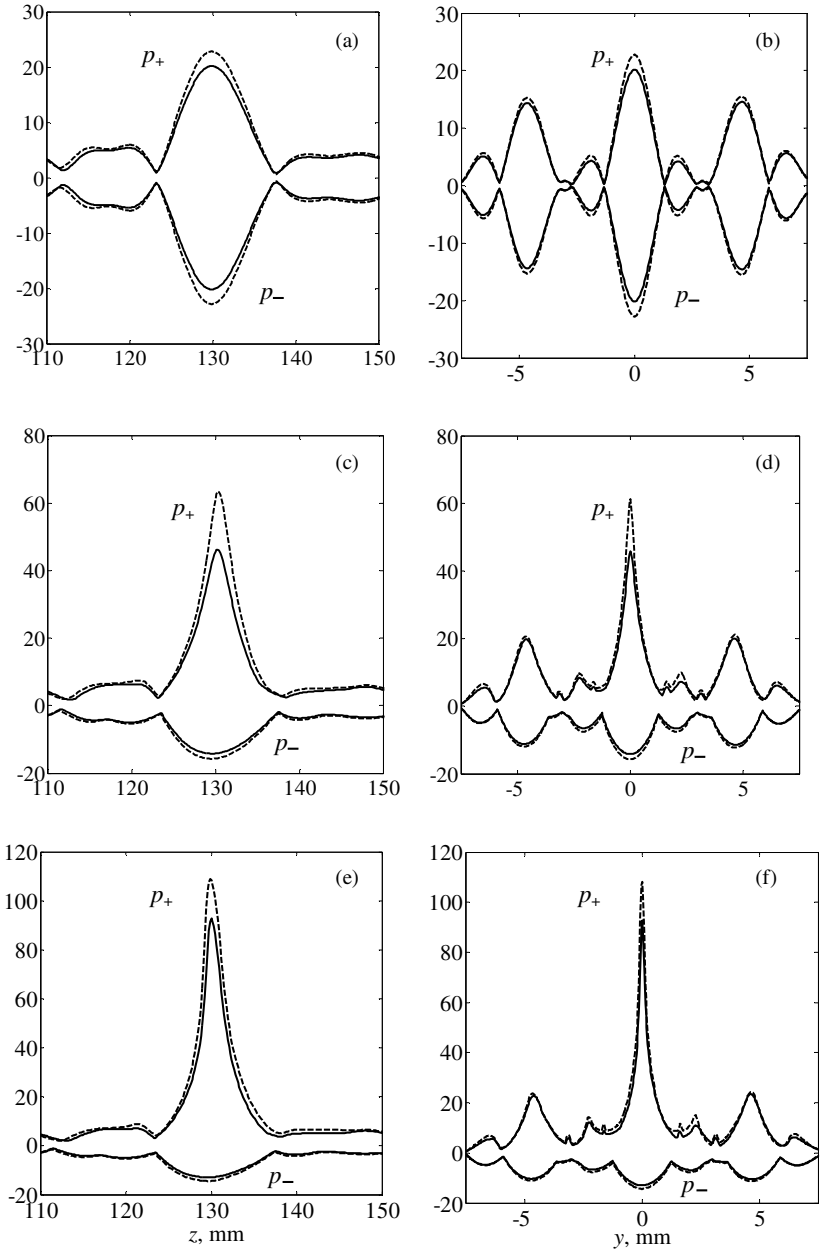

Figure 8. Peak positive and peak negative pressure distributions along the z-axis (left column) and in the focal plane (right column) along the y-axis ($x = 0$) when all the elements of the array are active (dashed lines) and when some elements are switched off (solid lines). The distributions are calculated using the linear approximation (a, b) and accounting for nonlinear effects at $I_0 =$ 20 W cm^{-2} (c, d) and $I_0 = 40$ W cm^{-2} (e, f). I_0 is the intensity at the operating array element front face. The distributions are normalized by the initial pressure amplitude $p_0 = \rho_0 c_0 V_0$.

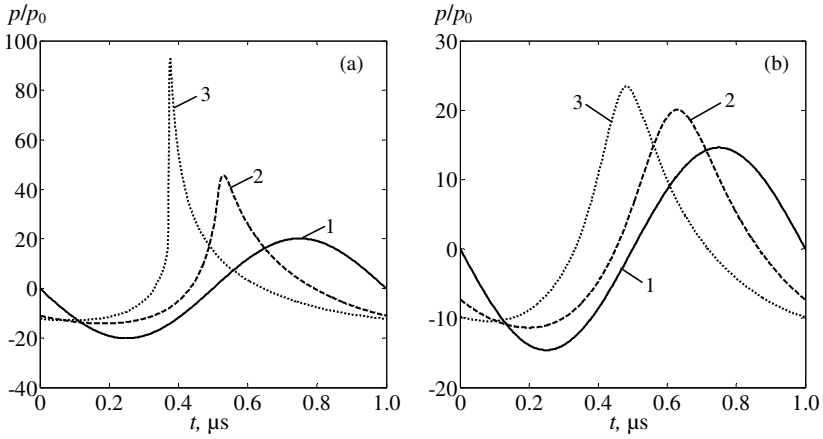

Figure 9. Pressure waveforms calculated in the main focus at (0, 0, 130 mm) (a) and in the secondary focus at (0, 4.6, 130 mm) (b) for linear beam focusing (curves 1) and accounting for nonlinear effects for $I_0 = 20$ W cm^{-2} (curves 2) and $I_0 = 40$ W cm^{-2} (curves 3). Some elements of the array are switched off to prevent rib heating. The waveforms are normalized to the initial pressure amplitude at the array elements.

((a),(b)), both peak pressures have lower values in the main and secondary foci in the case when the array operates with some elements switched off.

The degree of nonlinear effects is more obvious from the analysis of the waveforms in the corresponding focal regions. The waveforms calculated in the main and secondary foci at the points (0, 0, 130 mm) and (0, 4.6, 130 mm) are shown in figure 9 for the linear and two nonlinear ($I_0 = 20$ and 40 W cm^{-2}) beam focusing conditions, as in figure 8. The configuration when some elements of the array are switched off is considered. It is seen that the shock is present in the waveform in the main focus for $I_0 = 40$ W cm^{-2}. At the lower source output ($I_0 = 20$ W cm^{-2}), the focal waveform is distorted but not yet shocked. The waveforms in the secondary foci are only slightly distorted for both initial intensities of $I_0 = 20$ and 40 W cm^{-2}.

3.3. Nonlinear enhancement of tissue heating at the focus and suppression of side foci behind the ribs

Simulations of tissue heating behind the ribs were conducted for the array operating with some switched off elements. The ultrasound field and heat deposition rates in tissue were simulated using the linear and nonlinear acoustic models. The effect of enhanced heating due to the presence of shocks compared to linearly predicted heating was analysed over the range of initial intensities $I_0 = 2.5$, 5, 10, 20, 30 and 40 W cm^{-2}. The lowest value of $I_0 = 2.5$ W cm^{-2} was chosen on the basis of the experimental conditions for the *in vitro* tissue ablation considered in previous studies (Bobkova *et al* 2010, Ilyin *et al* 2011). Higher intensity values up to 40 W cm^{-2} where nonlinear effects became significant were chosen, as shown in figure 9. For nonlinear simulations focusing gain for intensity in nonlinear beams, $G_I = I_F/I_0$, increased by factors of 1.03, 1.05, 1.12, 1.3, 1.5 and 1.6 for $I_0 = 2.5$, 5, 10, 20, 30 and 40 W cm^{-2}, respectively, compared to the linearly predicted G_I.

The distributions of the heat deposition rates in tissue in a nonlinear beam along the z-axis (a) and in the focal plane along the y-axis (b) are shown in figure 10 for different initial intensities I_0. Continuous wave (cw) irradiation is considered; each curve is normalized

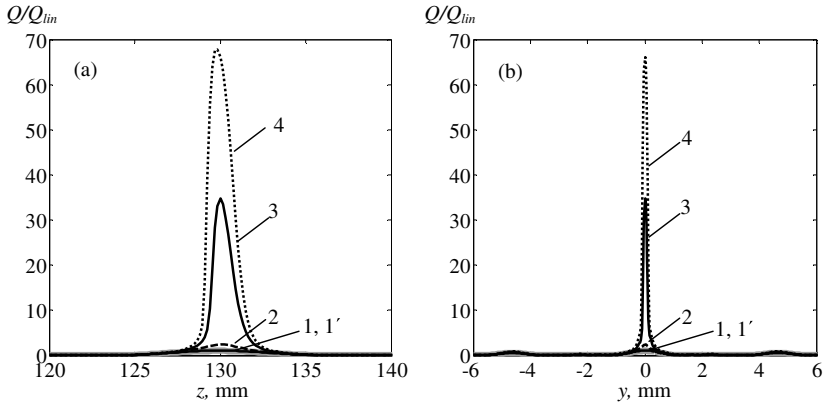

Figure 10. Distribution of heat deposition rate along the z-axis (a) and in the focal plane (b) along the y-axis ($x = 0$). The distributions were calculated using the linear approximation (grey bold curves 1) and accounting for nonlinearity for $I_0 = 2.5$ W cm^{-2} (1′), $I_0 = 20$ W cm^{-2} (2), $I_0 = 30$ W cm^{-2} (3) and $I_0 = 40$ W cm^{-2} (4).

by the corresponding heating rate in the focus calculated using the linear approximation of ultrasound propagation. In the case of low intensity, $I_0 = 2.5$ W cm^{-2} (curves 1 and 1′), the results of linear and nonlinear modelling are almost identical and thus the normalized peak heating rate in the main focus is equal to 1. At higher intensity $I_0 = 20$ W cm^{-2} a small increase in focal heating is observed relative to the linear predictions due to nonlinear generation and absorption of higher harmonics (curve 2). A sharp change occurs between initial intensities of 20 and 40 W cm^{-2} when shock fronts start to develop at the focus, and the heat deposition rate increases dramatically over the linear prediction (curves 3 and 4). For initial intensity $I_0 = 40$ W cm^{-2}, the heating rate calculated using the nonlinear model is 66 times higher than the heating calculated assuming linear propagation. In contrast, no enhancement of heating is observed in the secondary lobes, where pressures are lower and nonlinear effects weaker. The relative effect of heating in the secondary lobes is therefore strongly reduced in the case of nonlinear focusing through the ribs.

The effect of relative suppression of tissue heating in the secondary foci due to enhanced heating in the main focus is illustrated in more detail in figure 11 (upper row). The spatial distributions of heating rates in tissue are shown in the axial plane (yz) for different initial intensities at the array faces. The distributions are normalized here by the corresponding maximum value in the each plot. It is seen that with an increase of initial intensity from $I_0 = 2.5$ W cm^{-2} (a) to 5 W cm^{-2} (b) and 20 W cm^{-2} (c), the heated regions in tissue become smaller and the relative level of the side foci decreases. For intensities $I_0 = 30$ (d) and 40 W cm^{-2} (e), the heating rate distributions are highly localized. The spatial window in plots (d) and (e) along the y coordinate is reduced to the region around the main focus, as the levels of the side foci are negligible.

Temperature distributions in tissue for the same values of initial intensity I_0, and for nonlinear simulations, are presented in the middle row of figure 11 for the moment when the peak temperature in tissue reaches 100 °C. This temperature was reached in $t = 19$ s for $I_0 = 2.5$ W cm^{-2}; $t = 3.2$ s ($I_0 = 5$ W cm^{-2}); 740 ms ($I_0 = 10$ W cm^{-2}); 190 ms ($I_0 = 20$ W cm^{-2}); 9.5 ms ($I_0 = 30$ W cm^{-2}) and 2.5 ms ($I_0 = 40$ W cm^{-2}). The thermal dose is calculated at the same times and the corresponding contours of thermal lesions are shown in the bottom row of the figure. Again, cw exposures with a switched subset of elements are considered.

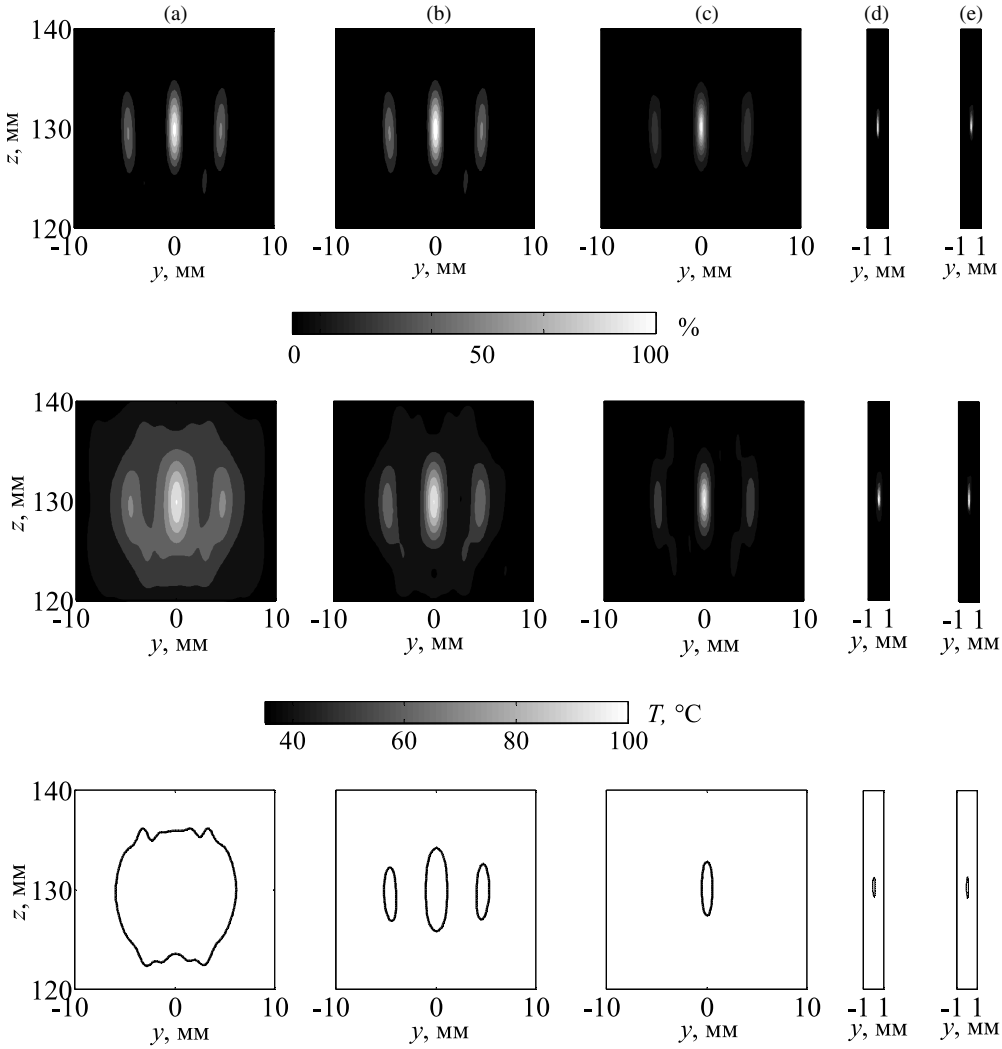

Figure 11. Spatial distributions of the heating rate $Q/Q_{\max}$ normalized to the maximum value of the corresponding distributions (upper row), temperature distributions T °C (middle row), and contours of thermal lesions in tissue (bottom row) at the time when the temperature in the centre of the main focus reaches 100 °C. Initial intensity at the array element front faces is $I_0 = 2.5$ W cm^{-2} (a), 5 W cm^{-2} (b), 20 W cm^{-2} (c), 30 W cm^{-2} (d), 40 W cm^{-2} (e).

For the lowest intensity and longest heating ($I_0 = 2.5$ W cm^{-2}, $t = 19$ s), the main and two-side heated regions merge due to heat diffusion and form one expanded lesion. This effect has also been observed in the experiments of the earlier study (Bobkova *et al* 2010) at the intensity output of the array shown in figure 12. In this case, the results of linear and nonlinear simulations are very close: for the linear (black curves) and nonlinear models (white curves) of heating the lesions are identical and show good agreement with the experiment (white colour in the images of tissue). Focal splitting is clearly observed in figure 11 in the temperature distributions for lesions formed for higher intensity and shorter heating times ($I_0 = 5$ W cm^{-2}, 3.2 s). With a further increase of intensity and decrease in heating time ($I_0 = 20$, 30 and

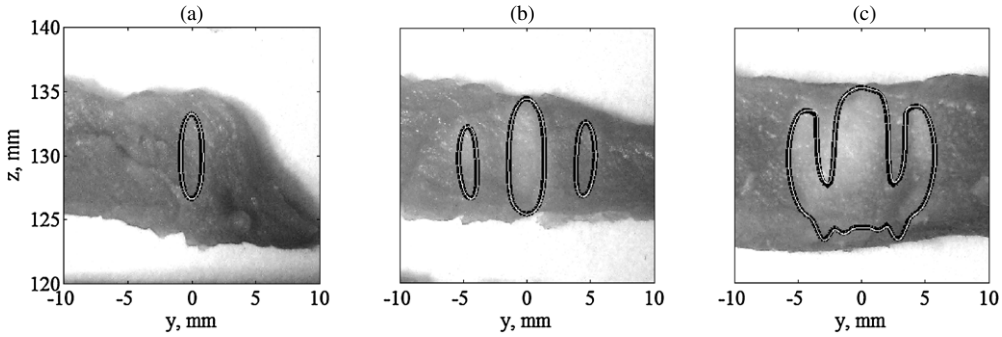

Figure 12. Contours of lesions modelled in the axial plane ($x = 0$) superimposed on the images of lesions produced in *ex vivo* tissue samples. The contours were calculated using linear (dark curves) and nonlinear (thin white curves) acoustic modelling at $I_0 = 2.5$ W cm^{-2} after 5 s (a), 10 s (b) and 15s (c) of heating.

Table 1. HIFU field parameters in a soft layer placed in the focal region behind the ribs. The array elements located in the shadow of ribs were switched off.

Initial intensity I_0 (W cm^{-2})	2.5 *	2.5	5	10	20	30	40
Initial pressure p_0 (MPa)	0.27	0.27	0.39	0.55	0.77	0.95	1.1
Focusing gain, $G_I = I_F/I_0$	367	377	387	410	476	552	580
Ratio of intensities in the main and side foci I_{main}/I_{side}	1.90	1.94	1.99	2.09	2.39	2.75	2.86
Focusing gain, $G_p = p_F/p_0$	19.2	23.5	26.2	31.8	50.9	77.1	80.8
Ratio of pressures in the main and side foci p_{main}/p_{side}	1.4	1.5	1.6	1.8	2.5	3.5	3.3
Ratio of linear and nonlinear heating rates in the main focus Q_N/Q_L	1.00	1.07	1.15	1.37	2.39	34.8	66.2
Ratio of heating rates in the main and side foci Q_{main}/Q_{side}	1.90	2.00	2.12	2.42	3.92	45.4	71.3
Time of achieving 100 °C in the main focus(ms)	19100	19000	3200	740	190	9.5	2.5
Ratio of temperature rise in the main and side foci when temperature in the main focus reaches 100 °C, $\Delta T_{main}/\Delta T_{side}$	1.79	1.82	2.00	2.20	3.00	26.0	65.0

The second column, marked as 2.5* W cm^{-2} for the initial intensity, corresponds to linear acoustic modelling; other initial values correspond to nonlinear modelling.

40 W cm^{-2}), the dimensions of the central lesion in the main focus become smaller and the side foci disappear. These results show that by using nonlinear effects, it is possible to heat very localized tissue volumes up to boiling temperatures within very short exposure times, and to reduce the relative level of heating in undesired hot spots that form in the case of the linear beam propagation through the ribs.

The results of modelling acoustic and temperature fields in tissue are summarized in table 1.

The previous figures have illustrated the nonlinear enhancement of tissue heating in the main focus, relative suppression of the side foci and reducing time to reach boiling temperatures for cw exposures. Recent studies have shown a growing interest in using pulse-periodic schemes that enable combined thermal and mechanical bioeffects in tissue when high peak intensities are used within pulses and thus nonlinear effects are present (Parsons *et al* 2006, Khokhlova *et al* 2011a). When irradiating through ribs, the use of such schemes (concentrating

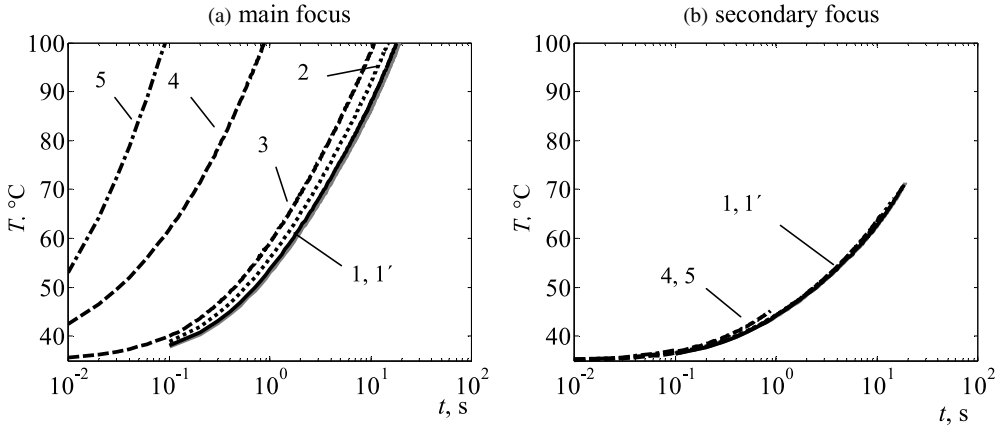

Figure 13. Temperature in the main focus (a) and in one of the split foci (b) against irradiation time for the same time-average, and different peak, intensities I_0 at the array elements: $I_0 = 2.5$ W cm^{-2} in continuous mode (1) and $I_0 = 10$ W cm^{-2} (2), $I_0 = 20$ W cm^{-2} (3), $I_0 = 30$ W cm^{-2} (4) and $I_0 = 40$ W cm^{-2} (5) in the pulse-periodic regimes. Curves 1–5 were simulated accounting for nonlinear effects, and curve 1′ was simulated linearly for $I_0 = 2.5$ W cm^{-2}.

acoustic power in a shorter pulse within a longer repetition period) provides additional benefits compared to continuous exposures with the same time-average power. While increasing the peak power in the pulse results in a significant nonlinear enhancement of heating in the focus, the ultrasound field in the rib plane is almost linear, and therefore no extra heating of ribs occurs. This situation is illustrated in figure 13 where the temperature rise over time at the main, and one of the side, foci is presented for the pulse-periodic irradiation regime with different peak intensity values I_0 and different pulse durations. The total energy irradiated within one pulse repetition period in the high-amplitude pulsing (nonlinear) regimes corresponds to the energy of continuous irradiation with an initial intensity $I_0 = 2.5$ W cm^{-2} (linear). The duty factor for intensity 20 W cm^{-2} is 0.125, and for 40 W cm^{-2} 0.0625. At lower peak intensity levels $I_0 \leqslant 20$ W cm^{-2}, when no shocks are present in the focal waveform, almost no difference is observed in the temperature curves in either the main or the secondary foci. With intensities of $I_0 = 30$ and 40 W cm^{-2}, shocks form in the main focus, leading to significant acceleration of the temperature rise in this position, and no increase in heating occurs in the secondary focus. With the same time-average intensity, tissue ablation in the focus is reached in less than 15 ms at 40 W cm^{-2} and 80 ms at 30 W cm^{-2} compared to 2 s for continuous exposure at 2.5 W cm^{-2}.

4. Discussion

Efficient tissue heating by shock waves has been shown to have some advantages in enhancing thermal effects in HIFU as well as in producing mechanical tissue disruption (Canney *et al* 2009, Khokhlova *et al* 2011a). However, no studies have yet been performed to evaluate the effects of shocks in tissue when using 2D multi-element HIFU arrays, and in the clinically important situation of sonicating through ribs. In this paper, nonlinear effects were studied in an HIFU field produced by a typical therapeutic phased array in a free field in water, in water in the presence of ribs and in a tissue layer behind the ribs. An array of 1 MHz frequency, 170 mm diameter, 130 mm focal length, consisting of 254 elements (focusing gain for pressure amplitude at low power output in water is $G_p = p_F/p_0 = 48$) was considered

(Hand *et al* 2009, Bobkova *et al* 2010). Nonlinear enhancement of tissue heating in the central focus, corresponding relative suppression of side foci caused by diffraction due to the periodic structure of ribs and different cw and pulse-periodic regimes of tissue heating were evaluated.

The results of numerical modelling showed that when nonlinear propagation effects were sufficiently strong to create shock fronts in the pressure waveforms in the focus in water, the peak positive pressure in the waveform was 100 MPa, peak negative pressure was 15 MPa and the shock front amplitude was 90 MPa (figure 3, curve 4). The initial intensity at the array elements in this case was 10 W cm^{-2} (0.55 MPa initial pressure). When irradiating through ribs, similar parameters were observed in the focal waveform at four times greater initial intensity of 40 W cm^{-2} (1.1 MPa pressure). As shown in figure 10, in the case of focusing in tissue in the presence of ribs at an initial intensity of 40 W cm^{-2} nonlinear heating of tissue is about 70 times greater than that for the case of linear propagation at the same initial intensity. This strong enhancement of heating can potentially be used to accelerate purely thermal ablation of tissue by fast steering of the focus over the heated volume, as well as to realize newer protocols of mechanical tissue emulsification based on rapid shock wave heating–boiling histotripsy (Canney *et al* 2009, Khokhlova *et al* 2011a). With an initial intensity of $I_0 = 40$ W cm^{-2}, boiling in tissue was reached after 2.5 ms of irradiation, which is about four orders of magnitude faster than for low output sonications: 19 s for $I_0 = 2.5$ W cm^{-2}. In addition to acceleration of tissue ablation, shorter shock wave exposures in *in vivo* clinical conditions (not considered here) would also reduce the effect of blood perfusion, thus leading to more predictable outcomes of the treatment.

An important advantage of using shock wave exposures while irradiating through ribs has been revealed in this study. It has been shown that at higher intensities the relative effect of heating tissue at additional side foci formed due to diffraction by the periodic structure of ribs is reduced significantly (figure 11). Nonlinear effects are amplitude dependent; they also accumulate with propagation distance through high-pressure regions. When the initial intensity at the array is sufficiently high that shocks form within the region of the main focus, nonlinear waveform distortion is almost negligible in the side foci of lower amplitude (figure 9). The relative effect of overheating unwanted tissue volumes is therefore reduced significantly. When modelling thermal effects at a 1 cm depth of focus in tissue, strong nonlinear effects in terms of localized enhancement of heating in the main focal lobe and relative suppression of side heated spots were observed for initial intensities higher than 30 W cm^{-2}. Although these effects are illustrated here for the side lobes formed due to diffraction by the regular structure of ribs, the same mechanism can be applied to other unwanted secondary hot spots in tissue, formed, for example, due to tissue inhomogeneities or electronic steering of the array focus. Extra nonlinear heating by shocks will occur in the region of the main focus only; thus, the relative thermal effect in other hot spots will be suppressed. This idea shows the potential for developing nonlinear HIFU irradiation protocols to produce confined lesions while better protecting overlying tissues, and ribs. As noted earlier in the introduction, a similar effect, but related to the value of the peak negative pressure, was recently observed for cavitation-cloud histotripsy lesions as long as the pressure in the main lobe exceeds the cavitation cloud initiation threshold and secondary lobes remain below the threshold (Kim *et al* 2011).

Moreover, since heating is enhanced in the main focus only, and not at the ribs where the field is almost linear, even sonications carried out without switching off the array elements may be applicable. Pulse-periodic schemes with high peak intensities and low duty factors, as illustrated in figure 13, can be used to create lesions in the focus while not overheating ribs. Similarly, the paper by Kim *et al* (2011) proposes that histotripsy can generate confined focal lesions through rib obstacles without aberration correction at the array because the threshold for cavitation cloud formation, which is the mechanism for tissue damage, is not

exceeded close to ribs. In addition to optimizing the array design, in some cases, when the mechanical movement of the transducer instead of electronic steering of the array focus is acceptable, an array can be substituted by a single-element source to use the total area of its surface for radiation and thus reach higher pressures in the focus necessary for shock formation.

The initial intensity values of 30–40 W cm^{-2} reported here to reach shocks with this specific array are about the maximum that current transducers can provide while ensuring their safety in terms of thermal or mechanical damage (Cathignol 2002, Fleury *et al* 2002). In the case of focusing deeper into tissue than in the current study, higher values of initial intensity will be needed to compensate for additional absorption to reach the same pressures at the focus. However, variation of the array parameters (frequency, sparseness, focal length and aperture) can decrease the threshold value of the array intensity required to produce shocks in the focus. For example, shock fronts form in the focus at half the initial intensity levels, at 5 W cm^{-2} for another typical HIFU array, operating at a slightly higher frequency (1.2 against 1 MHz) and with more compact distribution of the elements (64% against 40% area of the shell filled by the elements) (Yuldashev and Khokhlova 2011). The current trend is also to develop HIFU arrays with a larger number of elements (Marsac *et al* 2012) and more compact distribution (Raju *et al* 2011) which will lead to the same pressures at the focus for lower initial intensities. The potential to reach and utilize shock wave exposures in tissue using 2D arrays even in the presence of ribs is therefore realistic.

The Westervelt-type equation extended for the linear frequency law of absorption in tissue was shown to provide a useful model to evaluate nonlinear propagation effects in ultrasound fields generated by 2D HIFU arrays. Although the modelling is currently implemented to simulate forward ultrasound propagation only, i.e. does not account for the reflected waves, it still adequately captures the major bioeffects in tissue in the focal region. Nonlinear simulations, including the formation of shocks, have been validated against measurements in water for another 2D HIFU array with similar parameters (Kreider *et al* 2011) and shown good agreement. An acoustic model was combined here with the bioheat equation to model temperature rise in tissue, and thermally necrosed volumes were calculated based on the thermal dose formulation. The shapes of lesions predicted in the modelling showed good agreement with those previously obtained in *in vitro* experiments at low-power sonications. Previous studies of shock wave irradiation in simpler fields of single-element transducers using a KZK model in the absence of ribs have shown a good correlation between heating by shocks and predicted bioeffects in simulation and experiment. Further studies are planned to design and build a multi-element HIFU array to implement shock wave heating regimes experimentally in tissue, as well as to evaluate the ability of using single-element transducers without overheating ribs.

5. Conclusion

Numerical simulations based on the nonlinear Westervelt-type equation have shown that high-amplitude shock fronts can form at the focus of a multi-element focused therapeutic array at technically feasible intensity levels at the array elements while sonicating through ribs. The formation of shocks results in significant enhancement of tissue heating only in the main focus and the enhancement of heating was negligible in the side lobes of the field and at the ribs, where nonlinear effects are weak. Pulse-periodic exposures with high peak intensities and low duty cycle can be used to enhance thermal effects at the focus. As the total HIFU-on time to create a lesion using shock waves is significantly shorter, better protection of ribs can be provided even without additional aberration correction by the adjustment of the

operating parameters of the array elements. These results suggest that utilizing shocks can be beneficial to enable the rapid generation of precise and localized lesions in tissue while better protecting ribs and overlaying tissues. Additional optimization of parameters and the design of compact therapeutic arrays to provide maximum power outputs with lower intensity levels at its elements are necessary to achieve shock wave regimes for sonications deep in tissue.

Acknowledgments

This work was supported in part by the National Institute of Health (project no EB007643) and the Russian Foundation for Basic Research (project nos 12-02-00028, 12-02-31388, 13-02-00183). Numerical simulations were performed on the SKIF 'Chebyshev' and the 'Lomonosov' clusters of MSU supercomputer center. The authors gratefully acknowledge A Shaw and J Hand for help in getting experimental data for comparison with modelling and unfunded partnership with the European Metrology Research Programme (project no HLT03). They are particularly thankful to G ter Haar for the editorial comments and fruitful discussions.

References

Aubry J-F, Pernot M, Marquet F, Tanter M and Fink M 2008 Transcostal high-intensity-focused ultrasound: *ex vivo* adaptive focusing feasibility study *Phys. Med. Biol.* **53** 2937–51

Bailey M R, Khokhlova V A, Sapozhnikov O A, Kargl S G and Crum L A 2003 Physical mechanisms of the therapeutic effect of ultrasound *Acoust. Phys.* **49** 369–88

Bessonova O V, Khokhlova V A, Bailey M R, Canney M S and Crum L A 2009 Focusing of high power ultrasound beams and limiting values of shock wave parameters *Acoust. Phys.* **55** 463–73

Bessonova O V, Khokhlova V A, Canney M S, Bailey M R and Crum L A 2010 A derating method for therapeutic applications of high intensity focused ultrasound *Acoust. Phys.* **56** 376–85

Bobkova S, Gavrilov L, Khokhlova V, Shaw A and Hand J 2010 Focusing of high intensity ultrasound through the rib cage using therapeutic random phased array *Ultrasound Med. Biol.* **36** 888–906

Botros Y Y, Ebbini E S and Volakis J L 1998 Two-step hybrid virtual array-ray (VAR) technique for focusing through the rib cage *IEEE Trans. Ultrason. Ferroelectr. Freq. Control* **45** 989–99

Canney M S, Bailey M R, Crum L A, Khokhlova V A and Sapozhnikov O A 2008 Acoustic characterization of high intensity focused ultrasound fields: a combined measurement and modeling approach *J. Acoust. Soc. Am.* **124** 2406–20

Canney M, Khokhlova V, Hwang J H, Khokhlova T, Bailey M and Crum L 2009 Tissue erosion using shock wave heating and millisecond boiling in high intensity ultrasound field *Proc. 9th Int. Symp. on Therapeutic Ultrasound (Aix-En-Provence, France, 23–26 Sept.) AIP Conf. Proc.* **1215** 36–9

Canney M, Khokhlova V, Bessonova O, Bailey M and Crum L 2010 Shock-induced heating and millisecond boiling in gels and tissue due to high intensity focused ultrasound *Ultrasound Med. Biol.* **36** 250–67

Cathignol D 2002 High intensity piezoelectric sources for medical applications: technical aspects *Nonlinear Acoustics at the Beginning of the 21st Century: Proc. 16th ISNA (Moscow)* vol 1 ed OV Rudenko and O A Sapozhnikov (Moscow: Faculty of Physics, Moscow State University) pp 371–8

Civale J, Clarke R, Rivens I and ter Haar G 2006 The use of a segmented transducer for rib sparing in HIFU treatments *Ultrasound Med. Biol.* **32** 1753–61

Cochard E, Prada C, Aubry J F and Fink M 2009 Ultrasonic focusing through the ribs using the DORT method *Med. Phys.* **36** 3495–503

Crouzet S, Murat F J, Pasticier G, Cassier P, Chapelon J Y and Gelet A 2010 High intensity focused ultrasound (HIFU) for prostate cancer: current clinical status, outcomes and future perspectives *Int. J. Hyperth.* **26** 796–803

Daum D R and Hynynen K 1998 Thermal dose optimization via temporal switching in ultrasound surgery *IEEE Trans. Ultrason. Ferroelectr. Freq. Control* **45** 208–15

Dewey W C 1994 Arrhenius relationships from the molecule and cell to the clinic *Int. J. Hyperth.* **10** 457–83

Dubinsky T J, Cuevas C, Dighe M K, Kolokythas O and Hwang J H 2008 High-intensity focused ultrasound: current potential and oncologic applications *AJR. Am. J. Roentgenol.* **190** 191–9

Duck F A 1990 *Physical Properties of Tissue* (London: Academic) p 346

Filonenko E A, Gavrilov L R, Khokhlova V A and Hand J W 2004 Heating of biological tissues by two-dimensional phased arrays with random and regular element distributions *Acoust. Phys.* **50** 222–31

Filonenko E A and Khokhlova V A 2001 Effect of acoustic nonlinearity on heating of biological tissue induced by high intensity focused ultrasound *Acoust. Phys.* **47** 468–75

Fleury G, Berriet R, Le Baron O and Huguenin B 2002 New piezocomposite transducers for therapeutic ultrasound *2nd Int. Symp. on Therapeutic Ultrasound (Seattle)* vol 1 pp 428–36

Gavrilov L R and Hand J W 2000 A theoretical assessment of the relative performance of spherical phased arrays for ultrasound surgery *IEEE Trans. Ultrason. Ferroelectr. Freq. Control* **47** 125–39

Gélat P, ter Haar G and Saffari N 2011 Modelling of the acoustic field of a multi-element HIFU array scattered by human ribs *Phys. Med. Biol.* **56** 5553–81

Hand J W, Shaw A, Sadhoo N, Dickinson R J and Gavrilov L R 2009 Initial testing of a prototype phased array device for delivery of high intensity focused ultrasound (HIFU) *Phys. Med. Biol.* **54** 5675–93

Hesley G K, Gorny K R, Henrichsen T L, Woodrum D A and Brown D L 2008 A clinical review of focused ultrasound ablation with magnetic resonance guidance: an option for treating uterine fibroids *Ultrasound Q.* **24** 131–9

Hill C R, Bamber J C and ter Haar G (ed) 2004 *Physical Principles of Medical Ultrasonics* 2nd edn (West Sussex, UK: Wiley) p 431

Ilyin S A, Bobkova S M, Khokhlova V A and Gavrilov L R 2011 Simulation of thermal lesions in biological tissues irradiated by high-intensity focused ultrasound through the rib cage *Phys. Wave Phenom.* **19** 62–67

Kashcheeva S S, Sapozhnikov O A, Khokhlova V A, Averkiou M A and Crum L A 2000 Nonlinear distortion and attenuation of intense acoustic waves in lossy media obeying a frequency power law *Acoust. Phys.* **46** 170–7

Khokhlova T D, Canney M S, Khokhlova V A, Sapozhnikov O A, Crum L A and Bailey M R 2011a Controlled tissue emulsification produced by high intensity focused ultrasound shock waves and millisecond boiling *J. Acoust. Soc. Am.* **130** 3498–510

Khokhlova V A, Bailey M R, Reed J A, Cunitz B W, Kaczkowski P J and Crum L A 2006 Effects of nonlinear propagation, cavitation, and boiling in lesion formation by high intensity focused ultrasound in a gel phantom *J. Acoust. Soc. Am.* **119** 1834–48

Khokhlova V A, Bobkova S M and Gavrilov L R 2010 Focus splitting associated with propagation of focused ultrasound through the rib cage *Acoust. Phys.* **56** 665–74

Khokhlova V A, Souchon R, Tavakkoli J, Sapozhnikov O A and Cathignol D 2002 Numerical modeling of finite-amplitude sound beams: shock formation in the near field of a cw plane piston source *J. Acoust. Soc. Am.* **110** 95–108

Khokhlova V A, Yuldashev P V, Bobkova S M and Ilyin S A 2011b The role of nonlinear propagation effects in ablation of soft tissue behind the rib cage using a HIFU phased array *Proc. 11th Int. Symp. on Therapeutic Ultrasound (New York)* p 52

Kim Y, Wang T-Y, Zhen Xu and Cain C A 2011 Lesion generation through ribs using histotripsy therapy without aberration correction *IEEE Trans. Ultrason. Ferroelectr. Freq. Control* **58** 2334–43

Kreider W, Sapozhnikov O A, Farr N, Yuldashev P V, Partanen A, Brazzle D, Bailey M R, Kaczkowski P J and Khokhlova V A 2011 Acoustic holography and nonlinear modeling methods to characterize the Philips MR-guided HIFU source *Proc. 11th Int. Symp. on Therapeutic Ultrasound (New York)* p 41

Li F, Gong X, Hu K, Li C and Wang Z 2006 Effect of ribs in HIFU beam path on formation of coagulative necrosis in goat liver *Proc. 5th Int. Symp. on Therapeutic Ultrasound (Boston) AIP Conf. Proc.* **829** 477–80

Li J-L, Liu X-Z, Zhang D and Gong X-F 2007 Influence of ribs on the nonlinear sound field of therapeutic ultrasound *Ultrasound Med. Biol.* **33** 1413–20

Liu H-Li *et al* 2007 Feasibility of transrib focused ultrasound thermal ablation for liver tumors using a spherically curved 2D array: a numerical study *Med. Phys.* **34** 3436–48

Marsac L, Chauvet D, Larrat B, Pernot M, Robert B, Fink M, Boch A L, Aubry J F and Tanter M 2012 MR-guided adaptive focusing of therapeutic ultrasound beams in the human head *Med. Phys.* **39** 1141–9

Maxwell A D, Wang T-Y, Cain C A, Fowlkes J B, Sapozhnikov O A, Bailey M R and Xu Z 2011 Cavitation clouds created by shock scattering from bubbles during histotripsy *J. Acoust. Soc. Am.* **130** 1888–98

Meaney P M, Cahill M D and ter Haar G R 2000 The intensity dependence of lesion position shift during focused ultrasound surgery *Ultrasound Med. Biol.* **26** 441–50

O'Donnell M, Janes E T and Miller J G 1981 Kramers–Kronig relationship between ultrasonic attenuation and phase velocity *J. Acoust. Soc. Am.* **69** 696–701

Parsons J, Cain C, Abrams G and Fowlkes J 2006 Pulsed cavitational ultrasound therapy for controlled tissue homogenization *Ultrasound Med. Biol.* **32** 115–29

Press W H, Teukolsky S A, Vetterling W T and Flannery B P 2007 *Numerical Recipes in FORTRAN 77* 2nd edn (Cambridge: Cambridge University Press) pp 704–8

Quesson B, Merle M, Kohler M O, Mougenot C, Roujol S, de Senneville B D and Moonen C T 2010 A method for MRI guidance of intercostal high intensity focused ultrasound ablation in the liver *Med. Phys.* **37** 2533–40

Raju B I, Hall C S and Seip R 2011 Ultrasound therapy transducers with space-filling non-periodic arrays *IEEE Trans. Ultrason. Ferroelectr. Freq. Control* **58** 944–54

Ritchie R W, Leslie T, Phillips R, Wu F, Illing R, ter Haar G, Protheroe A and Cranston D 2010 Extracorporeal high intensity focused ultrasound for renal tumours: a 3-year follow-up *Br. J. Urol. Int.* **106** 1004–9

Sapareto S A and Dewey W C 1984 Thermal dose determination in cancer therapy *Int. J. Radiat. Oncol. Biol. Phys.* **10** 787–800

Westervelt P J 1963 Parametric acoustic array *J. Acoust. Soc. Am.* **35** 535–7

Wu F, Zhi-Biao W, Wen-Zhi C, Hui Z, Jin B, Jian-Zhong Z, Ke-Quan L, Cheng-Bing J, Fang-Lin X and Hai-Bing S 2004 Extracorporeal high intensity focused ultrasound ablation in the treatment of patients with large hepatocellular carcinoma *Ann. Surg. Oncol.* **11** 1061–9

Yuldashev P V and Khokhlova V A 2011 Simulation of three-dimensional nonlinear fields of ultrasound therapeutic arrays *Acoust. Phys.* **57** 334–43

Zemp R, Tavakkoli J and Cobbold R 2003 Modeling of nonlinear ultrasound propagation in tissue from array transducers *J. Acoust. Soc. Am.* **113** 139–52